This article has been accepted for inclusion in a future issue of this journal. Content is final as presented, with the exception of pagination.

Time-Domain Shielding Effectiveness Analysis Based on DGTD Method Accelerated by Local Time-Stepping and Parallel Techniques

Zheng Lang Jia, Huan Huan Zhang, *Senior Member, IEEE*, Da Zhi Ding, *Senior Member, IEEE*, Lei Zhao, *Senior Member, IEEE*, Qiang Ren, *Senior Member, IEEE*, and Li Jun Jiang, *Fellow, IEEE*

***Abstract*—The discontinuous Galerkin time-domain (DGTD) method accelerated by local time-stepping (LTS) and parallel techniques is employed to analyze the time-domain shielding effectiveness (TDSE) of metallic enclosures. The detailed formulations and implementation procedures of the DGTD method and LTS and parallel techniques are introduced. Numerical results validate the correctness of the proposed method. Moreover, the influence of various design parameters of the metallic enclosure, including aperture dimensions, wall thickness, spacing of aperture arrays, etc., on the TDSE are analyzed by the proposed method. Some rules are given for the design of the enclosure with rectangular apertures from the perspective of TDSE. The proposed method provides an extremely powerful tool for the evaluation of TDSE.**

***Index Terms*—Discontinuous Galerkin time-domain (DGTD) method, local time stepping (LTS), parallel technique, time-domain shielding effectiveness (TDSE).**

I. Introduction

With the rapid development of electronic information technology, various electronic equipment are widely applied in civil and military areas. These electronic equipment are usually sensitive to electromagnetic interference (EMI). Typical sources of EMI include various wireless devices, electrical equipment, high-speed digital electronics in civil area, radar, high-power microwave, and intensive electromagnetic pulse (EMP) in military area [1]. Electromagnetic shielding is an effective means to enhance the immunity of electronic equipment to EMI. A technical indicator named shielding effectiveness (SE) is adopted to evaluate the anti-EMI ability of a shielding enclosure [2].

The SE of a shielding enclosure is usually obtained through analytical calculation or numerical simulation during the design stage. Though the analytical calculation is simple and fast, it cannot be applied to complex enclosure structure under most circumstances [3], [4], [5], [6], [7]. The numerical simulation method has attracted a large number of researchers in recent years due to its universality and accuracy [8], [9], [10], [11], [12], [13], [14], [15], [16], [17], [18], [19], [20], [21]. There are several commonly used numerical methods: finite-difference time-domain (FDTD) method [8], [9], [10], [11], [12], [13], [14], finite-element method (FEM) [15], [16], and method of moments (MoM) [17], [18], [19], [20], [21]. For instance, the SE of the electromagnetic shielding fabrics was studied based on the FDTD method in [14]. The SE of braided shield cables is analyzed by using the FEM in [15]. In [18], the MoM was employed to evaluate the SE of a metallic enclosure subjected to direct and indirect lightning strikes.

Most of the aforementioned literature works focus on the simulation of the traditional SE defined in the frequency domain. If the time-domain numerical method like FDTD is utilized, the obtained transient fields need to be Fourier transformed to the frequency domain first. Then, the wideband SE at each frequency point can be calculated [11]. If the frequency-domain numerical methods, such as FEM and MoM, are employed, the SE at one frequency point can be computed at a time. However, the traditional frequency-domain SE is essentially only suitable for harmonic excitation. When the excitation is transient like an EMP signal, the traditional frequency-domain SE does not allow an immediate understanding and quantification of the effects of a shielding enclosure. Thus, the parameter of time-domain shielding effectiveness (TDSE) is proposed to tackle this problem [22], [23]. Since the TDSE is defined directly in the time domain based on the transient electromagnetic fields, the time-domain numerical method like FDTD is usually adopted [24], [25] to analyze the TDSE. It is worth mentioning that the classical FDTD method utilizes orthogonal grids for meshing, resulting in staircasing effects when modeling structures with curved surfaces. Although the conformal FDTD method can be used to accurately deal with the complex boundary [26], it is difficult

Manuscript received 11 September 2022; revised 16 December 2022; accepted 13 January 2023. This work was supported in part by the National Natural Science Foundation of China under Grant 62127812 and Grant 62025109 and in part by Fundamental Research Funds for the Central Universities under Grant JB210213. *(Corresponding author: Huan Huan Zhang.)*

Zheng Lang Jia and Huan Huan Zhang are with the National Key Laboratory of Antennas and Microwave Technology, Xidian University, Xi'an 710071, China (e-mail: 375580404@qq.com; zhanghuanajkd@outlook.com).

Da Zhi Ding is with the Department of Communication Engineering, Nanjing University of Science and Technology, Nanjing 210094, China (e-mail: dzding@njust.edu.cn).

Lei Zhao is with the School of Information and Control Engineering, China University of Mining and Technology, Xuzhou 221116, China (e-mail: leizhao@cumt.edu.cn).

Qiang Ren is with the School of Electronic and Information Engineering, Beihang University, Beijing 100191, China (e-mail: qiangren@buaa.edu.cn).

Li Jun Jiang is with the Department of Electrical and Electronic Engineering, University of Hong Kong, Hong Kong (e-mail: jianglj@hku.hk).

Color versions of one or more figures in this article are available at https://doi.org/10.1109/TEMC.2023.3239162.

Digital Object Identifier 10.1109/TEMC.2023.3239162

0018-9375 © 2023 IEEE. Personal use is permitted, but republication/redistribution requires IEEE permission.
See https://www.ieee.org/publications/rights/index.html for more information.

Authorized licensed use limited to: CHINA UNIVERSITY OF MINING AND TECHNOLOGY. Downloaded on February 02,2023 at 00:44:04 UTC from IEEE Xplore. Restrictions apply.

This article has been accepted for inclusion in a future issue of this journal. Content is final as presented, with the exception of pagination.

to implement this method. The discontinuous Galerkin time domain (DGTD) method has been proposed in recent years, which can utilize tetrahedral elements to accurately model arbitrarily shaped geometries like the finite-element-time domain (FETD) method [27], [28], [29]. Moreover, the DGTD method only needs to solve a small matrix equation related to each tetrahedron element, while a large global matrix equation related to all the elements is solved in the FETD method. Therefore, the DGTD method has advantages over the FETD method for large-scale problems in the consideration of limited computational resources.

A DGTD method with arbitrary order of accuracy in both space and time is proposed in [30]. The local time-stepping (LTS) technique is also adopted to enhance the speed of time-marching on multiscale problems. A partially staggered DGTD method, which has the advantages of conservation of energy, is spurious-free, and has optimal convergence, is proposed [31]. An exponential propagator is introduced to the DGTD method in [32], which is energy conserving when centered numerical flux is utilized. Considering the benefits of the DGTD method, it is utilized for the analysis of the TDSE of shielding enclosures. The contribution and novelty of this article can be summarized into two parts. On the one hand, the parallelized LTS-DGTD method is introduced in detail and implemented to accelerate the simulation process. The METIS software is employed to evenly group the meshes to balance the computations and reduce the communication among different processes [33]. On the other hand, the proposed method is applied to analyze the influence of various design parameters of the shielding enclosure, including aperture dimensions, wall thickness, spacing of aperture arrays, etc., on the TDSE. Some useful design rules for improving the TDSE are given in the conclusion.

II. Theories and Formulations

An incident wave is adopted to illuminate the metallic enclosures when the SE is analyzed. Thus, the scattered field is inevitably generated and fills the whole free space. Therefore, an absorbing boundary condition is needed to truncate the unbounded computational domain in the DGTD method. The uniaxial anisotropic perfectly matched layer is chosen to be the absorbing boundary condition in this article. As a result, the whole computational domain is divided into two regions, as shown in Fig. 1: PML region and non-PML region. In the following, the technical details of the proposed SE analysis method is introduced in four subsections, including the DGTD method for the non-PML region, the DGTD method for the PML region, the LTS method, and the parallel strategy of the whole algorithm.

A. DGTD Method for the Non-PML Region

The DGTD method starts from the Maxwell curl equations

$$\varepsilon \frac{\partial \mathbf{E}}{\partial t} = \nabla \times \mathbf{H} \tag{1}$$

$$\mu \frac{\partial \mathbf{H}}{\partial t} = -\nabla \times \mathbf{E} \tag{2}$$

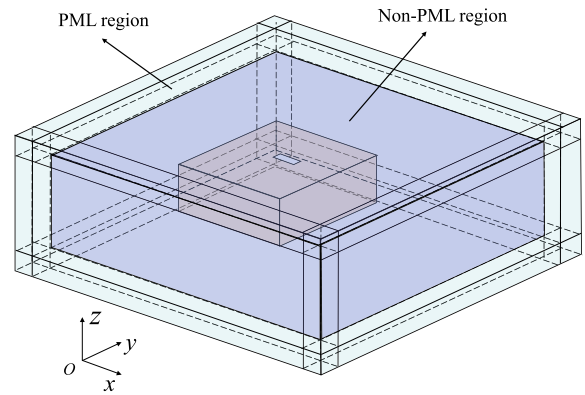

Fig. 1. 3-D computational domain for the SE analysis of metallic enclosures.

with permittivity ε and permeability μ.

The non-PML region is divided into N tetrahedral elements $V_1, V_2, ..., V_N$. The surface of the ith element is ∂V_i. By adopting Galerkin testing and vector identity transformation for (1) and (2), we can obtain

$$\int_{V_i} \varepsilon \mathbf{N}_k \cdot \frac{\partial \mathbf{E}}{\partial t} dV = \int_{V_i} \nabla \times \mathbf{N}_k \cdot \mathbf{H} dV + \int_{\partial V_i} \mathbf{N}_k \cdot (\hat{n} \times \mathbf{H}) dS \tag{3}$$

$$\int_{V_i} \mu \mathbf{N}_k \cdot \frac{\partial \mathbf{H}}{\partial t} dV = -\int_{V_i} \nabla \times \mathbf{N}_k \cdot \mathbf{E} dV - \int_{\partial V_i} \mathbf{N}_k \cdot (\hat{n} \times \mathbf{E}) dS \tag{4}$$

where $\mathbf{N}_k (k = 1, 2, \ldots, 20)$ refers to the second-order hierarchical vector basis functions [34], [35].

The upwind numerical flux is adopted by any pair of adjacent elements to calculate the surface integrals in (3) and (4). The expression of the upwind numerical flux is

$$\hat{n} \times \mathbf{H} = \hat{n} \times \mathbf{H}^i + \frac{Z^j}{Z^i + Z^j} \hat{n} \times (\mathbf{H}^j - \mathbf{H}^i) + \frac{1}{Z^i + Z^j} \hat{n} \times (\hat{n} \times (\mathbf{E}^i - \mathbf{E}^j)) \tag{5}$$

$$\hat{n} \times \mathbf{E} = \hat{n} \times \mathbf{E}^i + \frac{Y^j}{Y^i + Y^j} \hat{n} \times (\mathbf{E}^j - \mathbf{E}^i) + \frac{1}{Y^i + Y^j} \hat{n} \times (\hat{n} \times (\mathbf{H}^j - \mathbf{H}^i)) \tag{6}$$

where $Z^i = 1/Y^i = \sqrt{\mu^i/\varepsilon^i}$ and $Z^j = 1/Y^j = \sqrt{\mu^j/\varepsilon^j}$ are the wave impedance of the ith element and adjacent jth element, respectively.

Substituting (5), (6) into (3) and (4), and expanding the electric field and magnetic field with $\mathbf{N}_k (k = 1, 2, \ldots, 20)$, we can obtain the matrix equations after spatial discretization

$$\varepsilon \mathbf{M}^i \frac{\partial \mathbf{e}^i}{\partial t} = \mathbf{S}^i \mathbf{h}^i + \mathbf{F}_{ee}^{ii} \mathbf{e}^i - \mathbf{F}_{ee}^{ij} \mathbf{e}^j - \mathbf{F}_{eh}^{ii} \mathbf{h}^i + \mathbf{F}_{eh}^{ij} \mathbf{h}^j \tag{7}$$

Authorized licensed use limited to: CHINA UNIVERSITY OF MINING AND TECHNOLOGY. Downloaded on February 02,2023 at 00:44:04 UTC from IEEE Xplore. Restrictions apply.

This article has been accepted for inclusion in a future issue of this journal. Content is final as presented, with the exception of pagination.

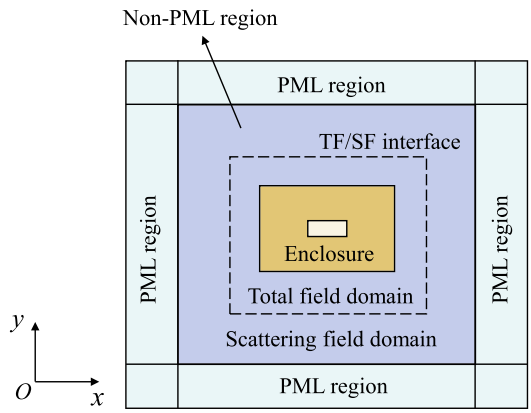

Fig. 2. 2-D computational domain for the SE analysis of metallic enclosures.

$$\mu\mathbf{M}^i\frac{\partial\mathbf{h}^i}{\partial t} = -\mathbf{S}^i\mathbf{e}^i + \mathbf{F}_{hh}^{ii}\mathbf{h}^i - \mathbf{F}_{hh}^{ij}\mathbf{h}^j + \mathbf{F}_{he}^{ii}\mathbf{e}^i - \mathbf{F}_{he}^{ij}\mathbf{e}^j \tag{8}$$

where $\mathbf{e}^i$ and $\mathbf{h}^i$ are the time-dependent expanding coefficient vectors in the ith element. The detailed expressions of all the matrix elements involved in (7) and (8) can be found in the Appendix.

Then, applying the leapfrog temporal integration scheme to (7) and (8), the final matrix equations can be obtained as

$$\varepsilon\mathbf{M}^i\mathbf{e}_{n+1}^i = \varepsilon\mathbf{M}^i\mathbf{e}_n^i + \Delta\mathrm{t}\left[\mathbf{S}^i\mathbf{h}_{n+1/2}^i + \mathbf{F}_{ee}^{ii}\mathbf{e}_n^i - \mathbf{F}_{ee}^{ij}\mathbf{e}_n^j - \mathbf{F}_{eh}^{ii}\mathbf{h}_{n+1/2}^i + \mathbf{F}_{eh}^{ij}\mathbf{h}_{n+1/2}^j\right] \tag{9}$$

$$\mu\mathbf{M}^i\mathbf{h}_{n+3/2}^i = \mu\mathbf{M}^i\mathbf{h}_{n+1/2}^i + \Delta\mathrm{t}\left[-\mathbf{S}^i\mathbf{e}_{n+1}^i + \mathbf{F}_{hh}^{ii}\mathbf{h}_{n+1/2}^i - \mathbf{F}_{hh}^{ij}\mathbf{h}_{n+1/2}^j + \mathbf{F}_{he}^{ii}\mathbf{e}_{n+1}^i - \mathbf{F}_{he}^{ij}\mathbf{e}_{n+1}^j\right]. \tag{10}$$

As shown in Fig. 2, the non-PML region consists of a total field (TF) area and a scattering field (SF) area. The incident waves $\mathbf{E}^{\text{inc}}$ and $\mathbf{H}^{\text{inc}}$ only exist in the TF area. The incident wave can be imposed by modifying the numerical flux. The numerical flux across the face lying on the TF/SF interface of an element in the TF area needs to change according to

$$\hat{n}\times\mathbf{E}^j = \hat{n}\times(\mathbf{E}^j + \mathbf{E}^{\text{inc}}) \tag{11}$$

$$\hat{n}\times\mathbf{H}^j = \hat{n}\times(\mathbf{H}^j + \mathbf{H}^{\text{inc}}). \tag{12}$$

The numerical flux across the face lying on the TF/SF interface of an element in the SF area needs to change according to

$$\hat{n}\times\mathbf{E}^j = \hat{n}\times(\mathbf{E}^j - \mathbf{E}^{\text{inc}}) \tag{13}$$

$$\hat{n}\times\mathbf{H}^j = \hat{n}\times(\mathbf{H}^j - \mathbf{H}^{\text{inc}}). \tag{14}$$

B. DGTD Method for the PML Region

The governing equations for the PML region include the Maxwell curl equations and two auxiliary equations [36]

$$\varepsilon\bar{\bar{a}}\cdot\frac{\partial\mathbf{E}}{\partial t} = -\varepsilon\bar{\bar{b}}\cdot\mathbf{E} - \varepsilon\bar{\bar{c}}\cdot\mathbf{p}^e + \nabla\times\mathbf{H} \tag{15}$$

$$\frac{\partial\mathbf{p}^h}{\partial t} = \bar{\bar{k}}^{-1}\cdot\mathbf{H} - \bar{\bar{d}}\cdot\mathbf{p}^h \tag{16}$$

$$\mu\bar{\bar{a}}\cdot\frac{\partial\mathbf{H}}{\partial t} = -\mu\bar{\bar{b}}\cdot\mathbf{H} - \mu\bar{\bar{c}}\cdot\mathbf{p}^h - \nabla\times\mathbf{E} \tag{17}$$

$$\frac{\partial\mathbf{p}^e}{\partial t} = \bar{\bar{k}}^{-1}\cdot\mathbf{E} - \bar{\bar{d}}\cdot\mathbf{p}^e \tag{18}$$

where the tensors $\bar{\bar{a}}$, $\bar{\bar{b}}$, $\bar{\bar{c}}$, $\bar{\bar{d}}$, and $\bar{\bar{k}}$ are all diagonal tensors with their first elements expressed as

$$a_{xx} = \frac{\kappa_y\kappa_z}{\kappa_x}, b_{xx} = \frac{(\sigma_y\kappa_z + \sigma_z\kappa_y - a_{xx}\sigma_x)}{\kappa_x\varepsilon}$$
$$c_{xx} = \frac{\sigma_y\sigma_z}{\varepsilon^2} - b_{xx}\frac{\sigma_x}{\varepsilon}, d_{xx} = \frac{\sigma_x}{\kappa_x\varepsilon}, k_{xx} = \kappa_x. \tag{19}$$

The expressions of the remaining elements of these tensors can be obtained by a simple permutation of the subscripts in (19). The values of κ_i and σ_i can be found in [37].

By adopting a similar derivation method in the non-PML region, we can obtain the matrix equations of the PML region after spatial discretization

$$\varepsilon\mathbf{T}_a^i\frac{\partial\mathbf{e}^i}{\partial t} = -\varepsilon\mathbf{T}_b^i\mathbf{e}^i - \varepsilon\mathbf{T}_c^i\mathbf{p}^e + \mathbf{S}^i\mathbf{h}^i - \mathbf{F}_{eh}^{ii}\mathbf{h}^i + \mathbf{F}_{ee}^{ii}\mathbf{e}^i + \mathbf{F}_{eh}^{ij}\mathbf{h}^j - \mathbf{F}_{ee}^{ij}\mathbf{e}^j \tag{20}$$

$$\mathbf{M}^i\frac{\partial\mathbf{p}^h}{\partial t} = \mathbf{T}_k^i\mathbf{h}^i - \mathbf{T}_d^i\mathbf{p}^h \tag{21}$$

$$\mu\mathbf{T}_a^i\frac{\partial\mathbf{h}^i}{\partial t} = -\mu\mathbf{T}_b^i\mathbf{h}^i - \mu\mathbf{T}_c^i\mathbf{p}^h - \mathbf{S}^i\mathbf{e}^i + \mathbf{F}_{he}^{ii}\mathbf{e}^i + \mathbf{F}_{hh}^{ii}\mathbf{h}^i - \mathbf{F}_{he}^{ij}\mathbf{e}^j - \mathbf{F}_{hh}^{ij}\mathbf{h}^j \tag{22}$$

$$\mathbf{M}^i\frac{\partial\mathbf{p}^e}{\partial t} = \mathbf{T}_k^i\mathbf{e}^i - \mathbf{T}_d^i\mathbf{p}^e. \tag{23}$$

The detailed expressions of all the matrix elements are given in the Appendix.

Again the leapfrog temporal integration scheme is applied to (20)–(23) to generate the fully discrete matrix equations of the PML region

$$\left(\varepsilon\mathbf{T}_a^i + \frac{\Delta t}{2}\varepsilon\mathbf{T}_b^i\right)\mathbf{e}_{n+1}^i = \left(\varepsilon\mathbf{T}_a^i - \frac{\Delta t}{2}\varepsilon\mathbf{T}_b^i\right)\mathbf{e}_n^i + \Delta t\left[-\varepsilon\mathbf{T}_c^i\mathbf{p}_{n+1/2}^e + \left(\mathbf{S}^i - \mathbf{F}_{eh}^{ii}\right)\mathbf{h}_{n+1/2}^i + \mathbf{F}_{eh}^{ij}\mathbf{h}_{n+1/2}^j + \mathbf{F}_{ee}^{ii}\mathbf{e}_n^i - \mathbf{F}_{ee}^{ij}\mathbf{e}_n^j\right] \tag{24}$$

$$\left(\mathbf{M}^i + \frac{\Delta t}{2}\mathbf{T}_d^i\right)\mathbf{p}_{n+1}^h = \Delta t\mathbf{T}_k^i\mathbf{h}_{n+1/2}^i + \left(\mathbf{M}^i - \frac{\Delta t}{2}\mathbf{T}_d^i\right)\mathbf{p}_n^h \tag{25}$$

Authorized licensed use limited to: CHINA UNIVERSITY OF MINING AND TECHNOLOGY. Downloaded on February 02,2023 at 00:44:04 UTC from IEEE Xplore. Restrictions apply.

This article has been accepted for inclusion in a future issue of this journal. Content is final as presented, with the exception of pagination.

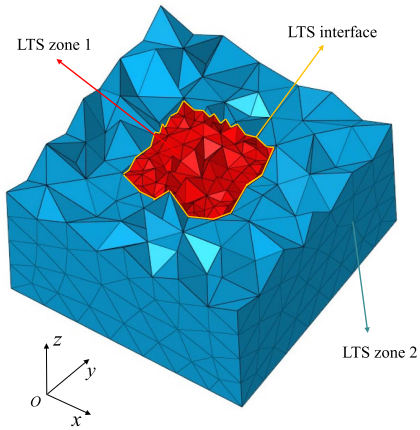

Fig. 3. LTS zones of the computational domain.

$$\left(\mu\mathbf{T}_a^i + \frac{\Delta t}{2}\mu\mathbf{T}_b^i\right)\mathbf{h}_{n+3/2}^i = \left(\mu\mathbf{T}_a^i - \frac{\Delta t}{2}\mu\mathbf{T}_b^i\right)\mathbf{h}_{n+1/2}^i + \Delta t\left[-\mu\mathbf{T}_c^i\mathbf{p}_{n+1}^h - \left(\mathbf{S}^i - \mathbf{F}_{he}^{ii}\right)\mathbf{e}_{n+1}^i - \mathbf{F}_{he}^{ii}\mathbf{e}_{n+1}^j + \mathbf{F}_{hh}^{ii}\mathbf{h}_{n+1/2}^i - \mathbf{F}_{hh}^{ij}\mathbf{h}_{n+1/2}^j\right] \tag{26}$$

$$\left(\mathbf{M}^i + \frac{\Delta t}{2}\mathbf{T}_d^i\right)\mathbf{p}_{n+3/2}^e = \Delta t\mathbf{T}_k^i\mathbf{e}_{n+1}^i + \left(\mathbf{M}^i - \frac{\Delta t}{2}\mathbf{T}_d^i\right)\mathbf{p}_{n+1/2}^e. \tag{27}$$

C. LTS Method

As an explicit difference method, the leapfrog temporal integration scheme is conditionally stable. The time step size is constrained by the minimal mesh size, so the computational efficiency of the DGTD method is low for multiscale problems. There always exist some fine structures like holes and slots in the metallic enclosures during SE analysis. In order to improve the computational efficiency, the LTS method is employed to handle the multiscale problems [38], [39], [40]. The LTS method is implemented in four steps. First, as shown in Fig. 3, the whole computational domain is partitioned into different LTS zones according to the physical dimensions of different parts. The zone with the smallest physical dimension is discretized with the finest mesh and marked as LTS zone 1, while other zones are discretized with coarser mesh and marked as LTS zone 2, LTS zone 3, etc.

Second, the local time step size Δt_i of the ith LTS zone is calculated according to the Courant–Friedrichs–Lewy condition and the smallest mesh size in the ith LTS zone [41]

$$c_i\Delta t_i\left[\frac{4\sqrt{5}}{3} + \frac{8}{3}\max\left(\sqrt{\frac{\mu_i}{\mu_j}}, \sqrt{\frac{\varepsilon_i}{\varepsilon_j}}\right)\right] < \frac{4V_i}{P_i} \tag{28}$$

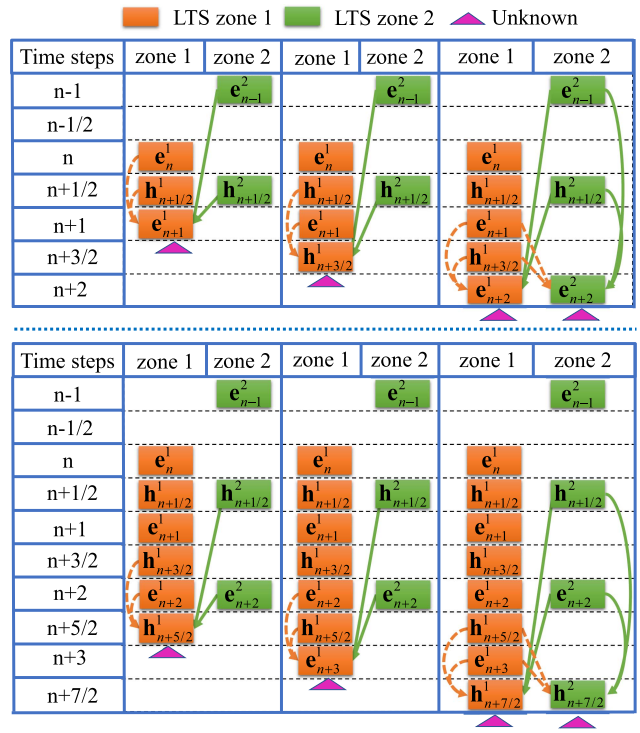

Fig. 4. LTS diagram at the interface of two groups.

where $c_i = 1/\sqrt{\varepsilon_i\mu_i}$ is the speed of light. The subscript j represents the neighboring element of the ith element. V_i is the volume of the smallest element in the ith LTS zone. P_i is the total area of the four faces of the element.

Third, the global time step Δt for the marching-on-in-time process of the DGTD method is set to be the minimal Δt_i, namely Δt_1. Then, the local time step $\Delta t_i (i = 2, 3, \ldots)$ is updated as a multiple of Δt, which is larger than its original value obtained by (28)

$$\Delta t_i = m_i\Delta t \tag{29}$$

where m_i is a strictly positive integer.

Finally, LTS is performed in different LTS zones. Take the computational domain with two LTS zones in Fig. 3 as an example; the mesh size in LTS zone 1 is small, while the mesh size in LTS zone 2 is large. According to the above three steps, m_i is set to be 3. Therefore, $\Delta t_1 = \Delta t$ and $\Delta t_2 = 3\Delta t$. Fig. 4 demonstrates the solution sequence of the LTS algorithm. According to (9) and (10), if the current electric field and magnetic field of an element are to be solved, the previous electric field and magnetic field of both the element and the adjacent element are needed. We will discuss the solution of the DGTD equations in the following four cases.

1) Both an element and its adjacent element are situated in LTS zone 1. The DGTD matrix equations of this element are solved with the time step size Δt. The previous electric field and magnetic field of the adjacent element are also obtained from LTS zone 1. This can be observed from the column of zone 1 in Fig. 4. Both the electric field and the magnetic field are updated with the time step size of Δt.

Authorized licensed use limited to: CHINA UNIVERSITY OF MINING AND TECHNOLOGY. Downloaded on February 02,2023 at 00:44:04 UTC from IEEE Xplore. Restrictions apply.

This article has been accepted for inclusion in a future issue of this journal. Content is final as presented, with the exception of pagination.

2) Both an element and its adjacent element are situated in LTS zone 2. The DGTD matrix equations of this element are solved with the time step size $3\Delta t$. The previous electric field and magnetic field of the adjacent element are also obtained from LTS zone 2. This can be observed from the column of zone 2 in Fig. 4. Both the electric field and the magnetic field are updated with the time step size of $3\Delta t$.
3) An element is in LTS zone 1, while its adjacent element is in LTS zone 2. These two elements are on the interface of zones 1 and 2. Compared with case 1), the DGTD matrix equations of this element are still solved with the time step size Δt. But the previous electric field and magnetic field of the adjacent element are obtained from LTS zone 2. Since the time step sizes of zones 1 and 2 are different, the needed electric field and magnetic field in zone 2 at certain time steps may be not available. Under this circumstances, the latest available previous electric field and magnetic field in zone 2 are utilized instead. For instance, in Fig. 4, the solution of $\mathbf{e}^1_{n+1}$, $\mathbf{h}^1_{n+3/2}$, and $\mathbf{e}^1_{n+2}$ are obtained by using $\mathbf{e}^2_{n-1}$ and $\mathbf{h}^2_{n+1/2}$ in zone 2.
4) An element is in LTS zone 2, while its adjacent element is in LTS zone 1. Compared with case 2), the DGTD matrix equations of this element are still solved with the time step size $3\Delta t$. But the previous electric field and magnetic field of the adjacent element are obtained from LTS zone 1. Again, the latest available previous electric field and magnetic field in zone 1 are utilized. For instance, in Fig. 4, the solution of $\mathbf{e}^2_{n+2}$ is obtained by using $\mathbf{e}^1_{n+1}$ and $\mathbf{h}^1_{n+3/2}$ in zone 1.

It is worth mentioning that the LTS method saves lots of computations in LTS zone 2 due to a large time step size. As shown in Fig. 4, in order to obtain $\mathbf{h}^1_{n+7/2}$ and $\mathbf{h}^2_{n+7/2}$ from $\mathbf{h}^1_{n+1/2}$ and $\mathbf{h}^2_{n+1/2}$, it needs to solve six times of equations for the elements in zone 1, while it only needs to solve two times of equations for the elements in zone 2.

D. LTS-DGTD Parallel Strategies

In order to further improve the computing speed, the message passing interface technique is utilized for the parallelization of the LTS-DGTD method. With the help of METIS software [33], the original mesh was evenly grouped to balance the computations among different processes. METIS is a freely distributed serial software package developed at the University of Minnesota, which contains a series of programs to implement multilevel graph partitioning algorithm. It can be utilized for effectively partitioning large irregular graphs, partitioning large meshes, etc. In this article, METIS is utilized to partition the original mesh into a specified number of groups and generate the METIS file. METIS can also guarantee that the number of elements at the interface of two adjacent groups is minimized to reduce the communication among different processes. The METIS file stores the partitioning of the elements, namely the mapping relation between the element number in original mesh and its corresponding group number. This group number is utilized later to decide which process will handle this element.

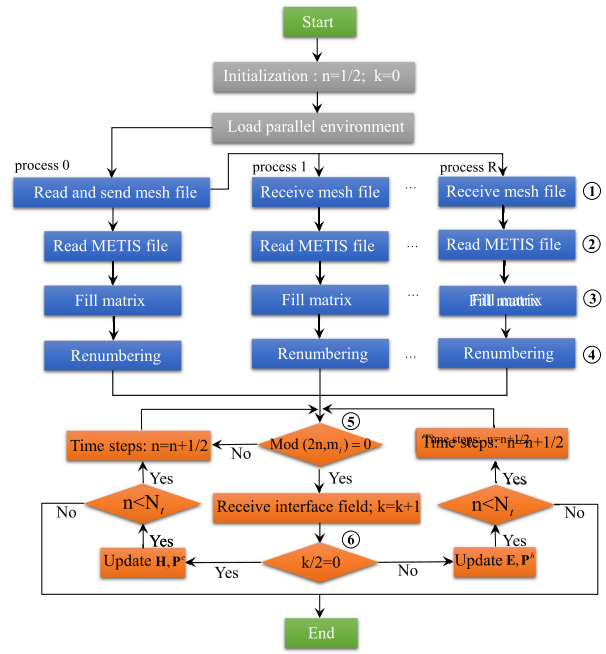

Fig. 5. Parallel strategies of the LTS-DGTD method.

Then, the parallel computing process of the LTS-DGTD method starts according to the parallel strategies in Fig. 5.

① The process 0 serves as the master process. It reads the mesh file and sends the mesh information to other processes.
② Each process reads the METIS file and determines which tetrahedral elements should be handled by itself.
③ Each process fills the matrices in (9) and (10) for elements in the non-PML region or in (24), (25), (26), and (27) for elements in the PML region.
④ Each process renumbers its own elements according to the LTS zones to build the mapping relation between the global element number and the local element number of some LTS zones.
⑤ For the elements in each LTS zone of every process, it is judged through the remainder operation $\mathrm{Mod}(2n,m_i) = 0$ whether the marching-on-in-time iterations of the DGTD equations are carried out.
⑥ A flag number k is utilized to control the alternating solution of electric field and magnetic field. According to (24) and (25), $\mathbf{P}^h$ and the electric field are solved together, while $\mathbf{P}^e$ is solved together with the magnetic field based on (26) and (27).

III. Numerical Results

At the beginning of this section, the performance of the proposed method is verified by the simulation of a metallic enclosure with a rectangular aperture. After that, various factors affecting the TDSE of the metallic enclosure are explored based on the proposed method. Unless otherwise specified, the numerical simulations are carried out on a workstation with Intel Xeon 8375c CPU with 64 cores and 512-GB RAM. Sixteen CPU cores are employed for parallel computing.

Authorized licensed use limited to: CHINA UNIVERSITY OF MINING AND TECHNOLOGY. Downloaded on February 02,2023 at 00:44:04 UTC from IEEE Xplore. Restrictions apply.

This article has been accepted for inclusion in a future issue of this journal. Content is final as presented, with the exception of pagination.

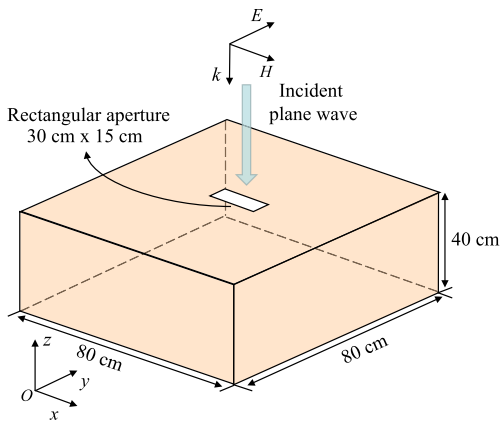

Fig. 6. Geometry of the metallic enclosure with a rectangular aperture.

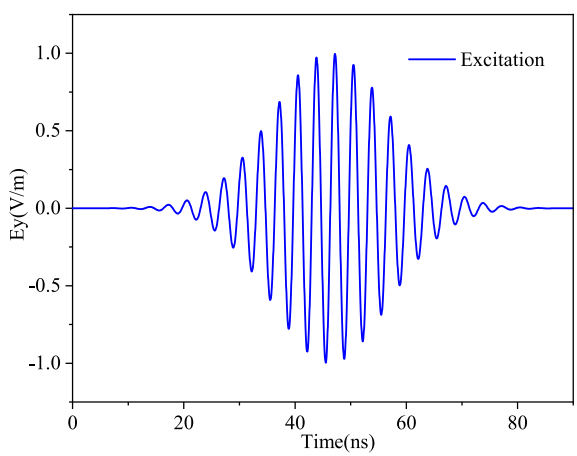

Fig. 7. Electric field intensity waveform of the incident plane wave.

TABLE I
NUMBER OF ELEMENTS AND TIME STEP SIZE OF THREE LTS ZONES

	Elements	Δt_i	m_i
LTS Zone 1	28783	4.5×10^{-13}s	1
LTS Zone 2	42921	1.8×10^{-12}s	4
LTS Zone 3	55929	7.2×10^{-12}s	16

A. Verification of the Proposed Method

As shown in Fig. 6, a 30 cm $\times$ 15 cm rectangular aperture is located in the center of the upper surface of the metallic enclosure. The length, width, and height of the enclosure are 80, 80, and 40 cm, respectively. The incident plane wave is along the negative z-axis. Its polarization direction is along the positive y-axis. As shown in Fig. 7, a modulated Gaussian pulse with an amplitude of 1 V/m is used as the excitation signal. Its center frequency is 300 MHz.

It is assumed that the enclosure has no thickness. Perfect electric conductor boundary condition is imposed on its surface. The whole computational domain is divided into three LTS regions, as shown in Fig. 8. LTS zone 1 includes the aperture, LTS zone 2 contains the enclosure, and the remaining is LTS zone 3. The number of elements, Δt_i and m_i, in each LTS zone

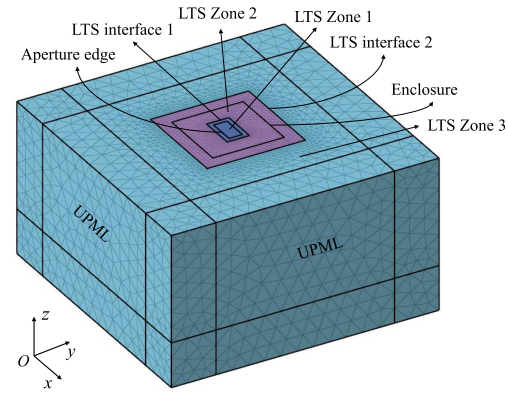

Fig. 8. LTS regions of the metallic enclosure.

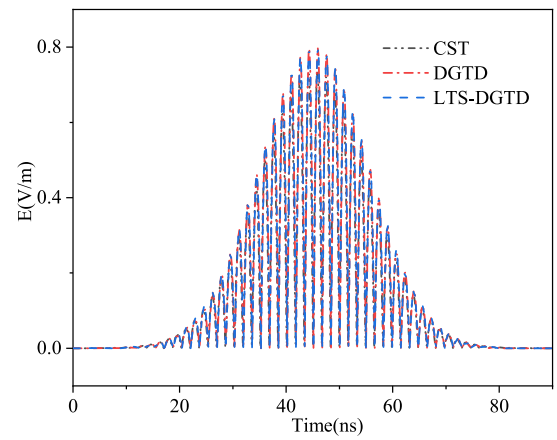

Fig. 9. Amplitude of the electric field intensity at the center of the enclosure obtained by different methods.

TABLE II
COMPARISON OF THE CPU TIMES OF DIFFERENT METHODS

CPU Time		
Sequential DGTD	Parallel DGTD	Parallel LTS-DGTD
419.5min	42.7min	17.1min

are given in Table I. The total simulation time is set to be 90 ns. The total number of time steps is 200 000.

The transient electric field at the center of the enclosure (0, 0, 0 mm) is calculated by the commercial software CST, traditional DGTD method, and the proposed method, as shown in Fig. 9. Good agreement can be observed. The time consumption is listed in Table II. Obviously, the proposed LTS-DGTD method can effectively shorten the simulation time by using LTS and parallel techniques. Therefore, the proposed method is adopted to accelerate the research on various factors affecting the TDSE of the metallic enclosure in the following. Besides, the size of the enclosure and the incident wave are the same with this example. The center of the enclosure is chosen to be the sampling point of the transient electric field in all the examples.

In order to assess the parallel performance of the proposed method, the relationship between the calculation time and the number of the CPU cores used in the parallel computation is given in Table III. The corresponding parallel efficiencies are

Authorized licensed use limited to: CHINA UNIVERSITY OF MINING AND TECHNOLOGY. Downloaded on February 02,2023 at 00:44:04 UTC from IEEE Xplore. Restrictions apply.

This article has been accepted for inclusion in a future issue of this journal. Content is final as presented, with the exception of pagination.

TABLE III
CPU TIME AND PARALLEL EFFICIENCY OF THE LTS-DGTD METHOD

Number of Processes	CPU Time (h)	Parallel Efficiency
4	22.8	100% (Baseline)
8	12.5	91.2%
16	6.4	89.1%
32	3.4	83.8%
48	2.6	73.1%

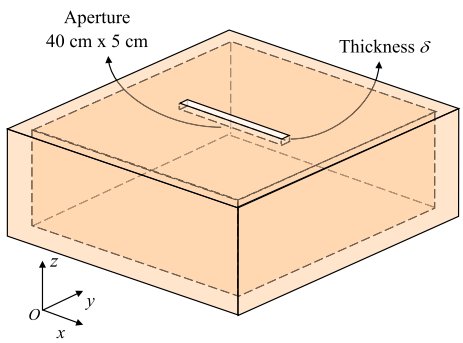

Fig. 10. Metallic enclosure with finite thickness δ.

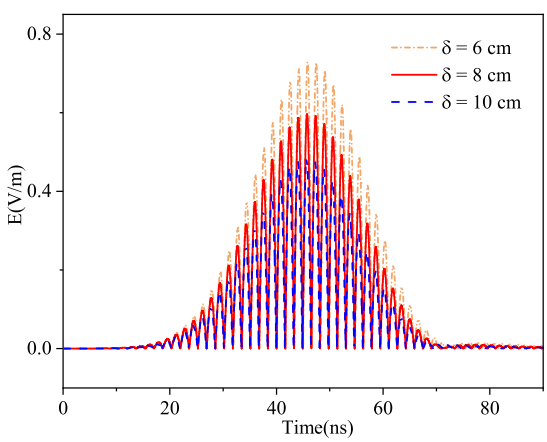

Fig. 11. Amplitude of the electric field intensity at the center of enclosures with different thicknesses.

also computed. It can be observed that the parallel performance of the proposed method is satisfactory.

B. Influence of Enclosure Thickness on TDSE

In the second example, the size of the rectangular aperture is fixed to be 40 cm × 5 cm, as shown in Fig. 10. The influence of enclosure thickness δ on the TDSE is studied. It is worth mentioning that the size of the inner wall of the enclosure is fixed when the enclosure thickness changes.

Fig. 11 presents the amplitudes of the transient electric fields at the center of the enclosure with the thicknesses of 6, 8, and 10 cm. It can be observed that the amplitude of the electric field decreases with the increase of the thickness. According to [23], three kinds of TDSE are defined as follows.

1) *Peak value reduction SE*

$$\mathrm{SE_{PR}} = 20\lg\frac{\left|\mathbf{E}^{\mathrm{in}}_{\mathrm{MAX}}(t,x,y,z)\right|}{\left|\mathbf{E}^{s}_{\mathrm{MAX}}(t,x,y,z)\right|} \tag{30}$$

TABLE IV
TDSE RESULTS INFLUENCED BY THE THICKNESS OF THE ENCLOSURE

Thickness	SE_{PR}	SE_{DR}	SE_{WR}
$\delta = 6$cm	2.72dB	−6.51dB	12.69dB
$\delta = 8$cm	4.45dB	−4.75dB	14.31dB
$\delta = 10$cm	6.33dB	−2.86dB	16.50dB

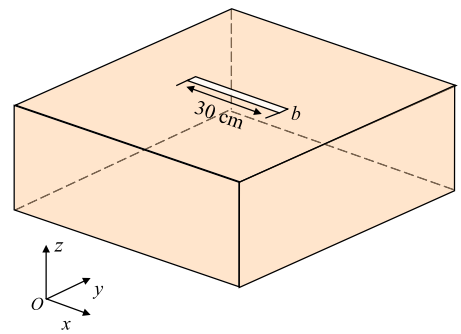

Fig. 12. Long side length of the aperture of a metallic enclosure is fixed.

where $\mathbf{E}^{\mathrm{in}}_{\mathrm{MAX}}(t,x,y,z)$ and $\mathbf{E}^{s}_{\mathrm{MAX}}(t,x,y,z)$ refer to the maximum values of the electric field at the observation point without and with the enclosure, respectively. The peak value reduction SE reflects the reduction of the peak value of the transient field in the shielded region.

2) *Derivative reduction SE*

$$\mathrm{SE_{DR}} = 20\lg\frac{\left|\dot{\mathbf{E}}^{\mathrm{in}}_{\mathrm{MAX}}(t,x,y,z)\right|}{\left|\dot{\mathbf{E}}^{s}_{\mathrm{MAX}}(t,x,y,z)\right|} \tag{31}$$

where $\dot{\mathbf{E}}^{\mathrm{in}}_{\mathrm{MAX}}(t,x,y,z)$ and $\dot{\mathbf{E}}^{s}_{\mathrm{MAX}}(t,x,y,z)$ are the maximum values of the time derivative of the electric field at the observation point without and with the enclosure, respectively. The derivative reduction SE reflects a reduction of the maximum time derivative of the transient field in the shielded region.

3) *Energy density reduction SE*

$$\mathrm{SE_{WR}} = 10\lg\frac{\left|W^{\mathrm{in}}(x,y,z)\right|}{\left|W^{s}(x,y,z)\right|} \tag{32}$$

where $W^{\mathrm{in}}(x,y,z)$ and $W^{s}(x,y,z)$ denote the energy at the observation point without and with the enclosure, respectively. The energy density reduction SE represents the reduction of the energy density flowing through the shielded region.

According to Table IV, all the three kinds of TDSE increase with the increment of the thickness. Based on Rodolfo Araneo's theory in [42], the source of radiation inside the metallic enclosure is reduced. Thus, the TDSE is increased.

C. Influence of the Short Side of the Rectangular Aperture on the TDSE

As shown in Fig. 12, the length of the long side of the rectangular aperture is fixed to be 30 cm. The length of the short side parallel to the direction of incident electric field is represented by parameter b. The influence of the length of the

Authorized licensed use limited to: CHINA UNIVERSITY OF MINING AND TECHNOLOGY. Downloaded on February 02,2023 at 00:44:04 UTC from IEEE Xplore. Restrictions apply.

This article has been accepted for inclusion in a future issue of this journal. Content is final as presented, with the exception of pagination.

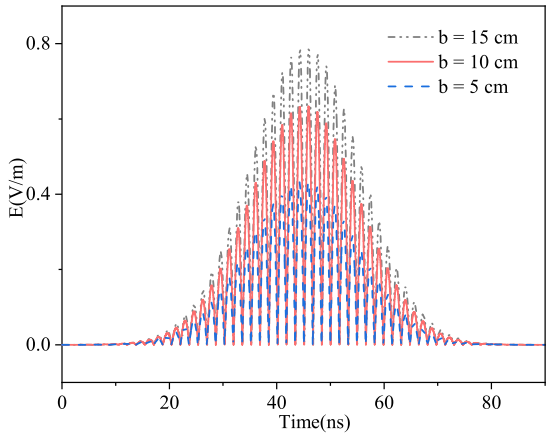

Fig. 13. Amplitude of the electric field intensity at the center of enclosures with different short side length of the aperture.

TABLE V
TDSE RESULTS INFLUENCED BY THE SHORT SIDE OF THE RECTANGULAR APERTURE

Short side	SE_{PR}	SE_{DR}	SE_{WR}
$b = 5$cm	7.27dB	-1.87dB	12.33dB
$b = 10$cm	3.94dB	-5.20dB	10.17dB
$b = 15$cm	2.01dB	-7.12dB	9.30dB

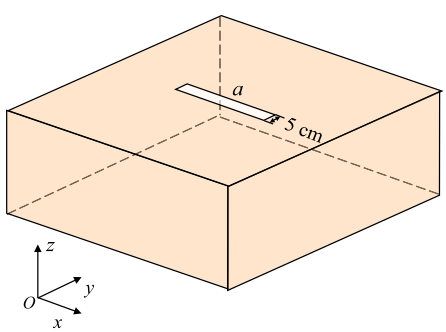

Fig. 14. Short side length of the aperture of a metallic enclosure is fixed.

short side on the TDSE is studied. Fig. 13 shows the amplitudes of the transient electric fields at the center of the enclosure when the length of the short side was 5, 10, and 15 cm, respectively. The amplitude of the electric field intensity at the observation point increases with the increment of b. The three kinds of TDSE are calculated, as shown in Table V. It can be concluded that the shorter the short side, the higher the TDSE. The rectangular aperture can be equivalent to an antenna. The reduction of its short side length is equivalent to the reduction of the effective receiving area of the antenna, which weakens the ability of the antenna to receive the energy of the incident wave. As a result, the electric field intensity entering the metallic enclosure becomes smaller and the TDSE increases.

D. Influence of the Long Side of the Rectangular Aperture on the TDSE

As shown in Fig. 14, the length of the short side of the rectangular aperture is fixed to be 5 cm. The length of the

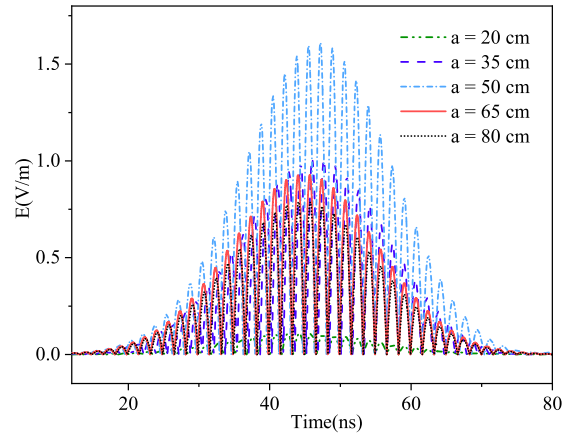

Fig. 15. Amplitude of the electric field intensity at the center of enclosures with different long side length of the aperture.

TABLE VI
TDSE RESULTS INFLUENCED BY THE LONG SIDE OF THE RECTANGULAR APERTURE

Long side	SE_{PR}	SE_{DR}	SE_{WR}
$a = 20$cm	19.33dB	12.76dB	26.43dB
$a = 35$cm	-0.09dB	-9.28dB	9.30dB
$a = 50$cm	-4.25dB	-13.14dB	5.75dB
$a = 65$cm	0.62dB	-8.36dB	12.51dB
$a = 80$cm	2.05dB	-6.96dB	14.08dB

long side is represented by parameter a. Fig. 15 shows the amplitudes of the transient electric fields at the center of the enclosure when the length of the long side was 20, 35, 50, 65, and 80 cm, respectively. It can be observed that the variation of the amplitude of the electric field is not monotonic with the length of the long side. More specifically, when the value of a is close to the half-wavelength of the incident wave (50 cm in this case), the amplitude of the electric field is the largest. The values of the three kinds of TDSE are calculated, as shown in Table VI. When $a = 50$ cm, the three kinds of TDSE are the lowest. A negative TDSE value indicates that the designed SE is even worse than that without a metallic enclosure. In conclusion, the TDSE becomes the worst as the length of the long side approaches the half-wavelength of the incident wave. This phenomenon can be explained by antenna theory. The rectangular aperture can also be equivalent to a slot antenna. When the long side perpendicular to the direction of incident electric field approaches the half-wavelength of the incident wave, the antenna works near the resonant mode. In this case, the radiation of the antenna is relatively large, leading to a small TDSE. Wang et al. [10] studied the coupling of electromagnetic waves into various slots or apertures numerically and presented the following universal equation for different kinds of slots:

$$f_r = \frac{c}{2l_{\max}} \tag{33}$$

where f_r is the frequency at which the resonant phenomenon takes place, and $l_{\max}$ is the largest length of slot in the direction perpendicular to the vector of the incident electric field. In our example, $l_{\max} = 50$ cm, so $f_r = 300$ MHz. The center frequency

Authorized licensed use limited to: CHINA UNIVERSITY OF MINING AND TECHNOLOGY. Downloaded on February 02,2023 at 00:44:04 UTC from IEEE Xplore. Restrictions apply.

This article has been accepted for inclusion in a future issue of this journal. Content is final as presented, with the exception of pagination.

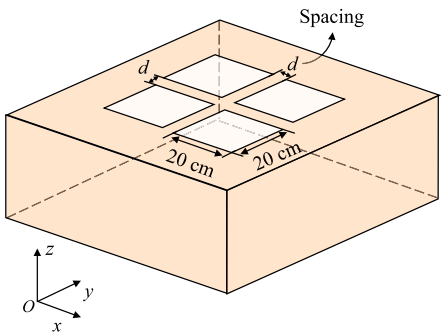

Fig. 16. Metallic enclosure with the spacing d between the apertures.

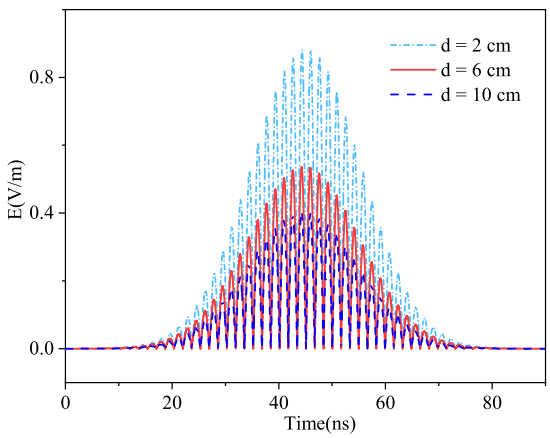

Fig. 17. Amplitude of the electric field intensity at the center of enclosures with different spacing between apertures.

TABLE VII
TDSE RESULTS INFLUENCED BY THE SPACING OF APERTURE ARRAY ELEMENTS

Spacing	SE_{PR}	SE_{DR}	SE_{WR}
$d = 2$cm	1.07dB	-8.06dB	8.33dB
$d = 6$cm	5.38dB	-3.72dB	13.17dB
$d = 10$cm	7.89dB	-1.20dB	15.60dB

of the incident wave in our numerical example agrees well with the resonant frequency f_r calculated by (33).

E. Influence of Spacing of Aperture Arrays on the TDSE

As shown in Fig. 16, the influence of the spacing between the apertures of a 2×2 aperture array is studied. The size of the aperture is 20 cm $\times$ 20 cm. The aperture spacing d is the same along the x and y directions. Fig. 17 shows the amplitude of the transient electric fields at the center of the enclosure when the spacing of apertures was 2, 6, and 10 cm, respectively. The values of TDSE are calculated as shown in Table VII, which increase with the enlargement of d. According to [43], the increase of spacing reduces the coupling between holes. As a result, the field entering the metallic enclosure is also reduced and the TDSE is improved.

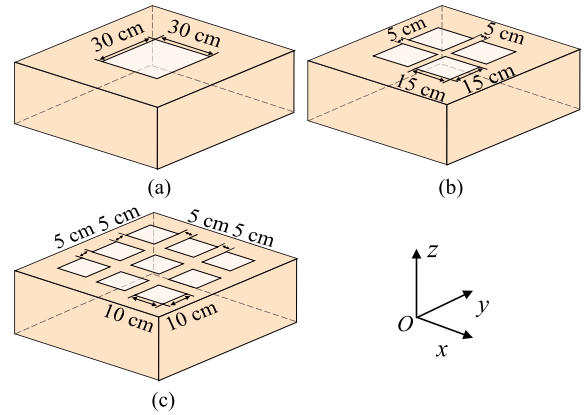

Fig. 18. Metallic enclosure with different aperture arrays. (a) 1×1. (b) 2×2. (c) 3×3.

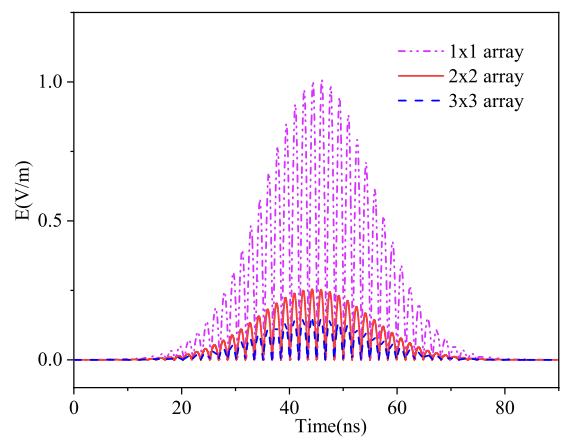

Fig. 19. Amplitude of the electric field intensity at the center of enclosures with different aperture arrays.

TABLE VIII
TDSE RESULTS INFLUENCED BY THE NUMBER OF APERTURE ARRAY ELEMENTS

Array	SE_{PR}	SE_{DR}	SE_{WR}
1×1	-0.09dB	-9.21dB	6.75dB
2×2	11.88dB	-2.80dB	19.84dB
3×3	16.60dB	-10.04dB	24.22dB

F. Influence of the Number of Aperture Elements on the TDSE

In the last example, the influence of the number of array elements of the rectangular aperture array on the TDSE is studied. As shown in Fig. 18, the total area of the hole is 900 cm^2. The number of array elements is 1×1, 2×2, and 3×3, respectively. The spacings between holes are fixed to be 5 cm. Fig. 19 shows the amplitudes of the transient electric fields at the center of the enclosure with the variation of the number of array elements. With the increment of the number of apertures, the field entering the metallic enclosure becomes small. The values of the three kinds of TDSE are summarized in Table VIII. Since the total area of the aperture array is fixed, the increase of the number of array elements will decrease the area of each aperture and, thus, increase the SE_{PR} and SE_{WR}. But the SE_{DR} of the 2×2 array is the highest, which means the time derivative of

Authorized licensed use limited to: CHINA UNIVERSITY OF MINING AND TECHNOLOGY. Downloaded on February 02,2023 at 00:44:04 UTC from IEEE Xplore. Restrictions apply.

This article has been accepted for inclusion in a future issue of this journal. Content is final as presented, with the exception of pagination.

the electric field at the observation point with the enclosure is the smallest in this case.

IV. Conclusion

The DGTD method was utilized for the analysis of the TDSE of a metallic enclosure in this article. The LTS and parallel techniques were adopted to accelerate the simulation. The proposed method provided an effective and powerful tool for electromagnetic shielding simulation. A series of widely recognized rules of SE in the frequency domain were also studied in the time domain through the proposed method. The following rules are given for the design of the enclosure with rectangular apertures from the perspective of TDSE.

1) A better shielding effect can be obtained by appropriately increasing the thickness of the metallic enclosure.
2) When designing rectangular apertures, the shorter the side length, the greater the TDSE. But it should be avoided that the side length is close to the half-wavelength of the incident wave.
3) For a certain number of array apertures, reasonably increasing the spacing between apertures can achieve better shielding effect.
4) When the total area of apertures is fixed, increasing the number of array elements can improve SE_{PR} and SE_{WR}. But SE_{DR} does not monotonically change with the number of array elements.

Appendix

$$\left[\mathbf{M}^i\right]_{kl} = \int_{V_i} \mathbf{N}_k^i \cdot \mathbf{N}_l^i dV \tag{34}$$

$$\left[\mathbf{S}^i\right]_{kl} = \int_{V_i} \mathbf{N}_k^i \cdot (\nabla \times \mathbf{N}_l^i) dV \tag{35}$$

$$\left[\mathbf{F}_{eh}^{ii}\right]_{kl} = \frac{Z^j}{Z^i + Z^j} \int_{\partial V_i} \mathbf{N}_k^i \cdot (\hat{n} \times \mathbf{N}_l^i) dS \tag{36}$$

$$\left[\mathbf{F}_{eh}^{ij}\right]_{kl} = \frac{Z^j}{Z^i + Z^j} \int_{\partial V_i} \mathbf{N}_k^i \cdot (\hat{n} \times \mathbf{N}_l^j) dS \tag{37}$$

$$\left[\mathbf{F}_{he}^{ii}\right]_{kl} = \frac{Y^j}{Y^i + Y^j} \int_{\partial V_i} \mathbf{N}_k^i \cdot (\hat{n} \times \mathbf{N}_l^i) dS \tag{38}$$

$$\left[\mathbf{F}_{he}^{ij}\right]_{kl} = \frac{Y^j}{Y^i + Y^j} \int_{\partial V_i} \mathbf{N}_k^i \cdot (\hat{n} \times \mathbf{N}_l^j) dS \tag{39}$$

$$\left[\mathbf{F}_{ee}^{ii}\right]_{kl} = \frac{1}{Z^i + Z^j} \int_{\partial V_i} \mathbf{N}_k^i \cdot (\hat{n} \times \hat{n} \times \mathbf{N}_l^i) dS \tag{40}$$

$$\left[\mathbf{F}_{ee}^{ij}\right]_{kl} = \frac{1}{Z^i + Z^j} \int_{\partial V_i} \mathbf{N}_k^i \cdot (\hat{n} \times \hat{n} \times \mathbf{N}_l^j) dS \tag{41}$$

$$\left[\mathbf{F}_{hh}^{ii}\right]_{kl} = \frac{1}{Y^i + Y^j} \int_{\partial V_i} \mathbf{N}_k^i \cdot (\hat{n} \times \hat{n} \times \mathbf{N}_l^i) dS \tag{42}$$

$$\left[\mathbf{F}_{hh}^{ij}\right]_{kl} = \frac{1}{Y^i + Y^j} \int_{\partial V_i} \mathbf{N}_k^i \cdot (\hat{n} \times \hat{n} \times \mathbf{N}_l^j) dS \tag{43}$$

$$\left[\mathbf{T}_a^i\right]_{kl} = \int_{V_i} \mathbf{N}_k^i \cdot \overline{\overline{a}} \cdot \mathbf{N}_l^i dV \tag{44}$$

$$\left[\mathbf{T}_b^i\right]_{kl} = \int_{V_i} \mathbf{N}_k^i \cdot \overline{\overline{b}} \cdot \mathbf{N}_l^i dV \tag{45}$$

$$\left[\mathbf{T}_c^i\right]_{kl} = \int_{V_i} \mathbf{N}_k^i \cdot \overline{\overline{c}} \cdot \mathbf{N}_l^i dV \tag{46}$$

$$\left[\mathbf{T}_d^i\right]_{kl} = \int_{V_i} \mathbf{N}_k^i \cdot \overline{\overline{d}} \cdot \mathbf{N}_l^i dV \tag{47}$$

$$\left[\mathbf{T}_k^i\right]_{kl} = \int_{V_i} \mathbf{N}_k^i \cdot \overline{\overline{k}}^{-1} \cdot \mathbf{N}_l^i dV. \tag{48}$$

References

[1] W. A. Radasky and R. Hoad, "Recent developments in high power EM (HPEM) standards with emphasis on high altitude electromagnetic pulse (HEMP) and intentional electromagnetic interference (IEMI)," *IEEE Lett. Electromagn. Compat. Pract. Appl.*, vol. 2, no. 3, pp. 62–66, Sep. 2020.

[2] A. Shourvarzi and M. Joodaki, "Shielding effectiveness estimation of a metallic enclosure with an aperture using S-parameter analysis: Analytic validation and experiment," *IEEE Trans. Electromagn. Compat.*, vol. 59, no. 2, pp. 537–540, Apr. 2017.

[3] H. A. Bethe, "Theory of diffraction by small holes," *Phys. Rev.*, vol. 66, pp. 163–182, Oct. 1944.

[4] M. P. Robinson et al., "Analytical formulation for the shielding effectiveness of enclosures with apertures," *IEEE Trans. Electromagn. Compat.*, vol. 40, no. 3, pp. 240–248, Aug. 1998.

[5] B. L. Nie, Q. S. Liu, and P. A. Du, "An improved thickness correction method of analytical formulations for shielding effectiveness prediction," *IEEE Trans. Electromagn. Compat.*, vol. 58, no. 3, pp. 907–910, Jun. 2016.

[6] E. Liu, P. A. Du, and B. Nie, "An extended analytical formulation for fast prediction of shielding effectiveness of an enclosure at different observation points with an off-axis aperture," *IEEE Trans. Electromagn. Compat.*, vol. 56, no. 3, pp. 589–598, Jun. 2014.

[7] B. L. Nie, P. A. Du, and P. Xiao, "An improved circuital method for the prediction of shielding effectiveness of an enclosure with apertures excited by a plane wave," *IEEE Trans. Electromagn. Compat.*, vol. 60, no. 5, pp. 1376–1383, Oct. 2018.

[8] M. S. Sarto, "A new model for the FDTD analysis of the shielding performances of thin composite structures," *IEEE Trans. Electromagn. Compat.*, vol. 41, no. 4, pp. 298–306, Nov. 1999.

[9] L. Yan et al., "Efficient shielding effectiveness prediction of metallic structures with three-dimensional arbitrary thin slots using extended CP-FDTD," *IEEE Trans. Electromagn. Compat.*, vol. 61, no. 4, pp. 1353–1361, Aug. 2019.

[10] J. Wang, G. Liu, and J. Zhou, "Investigations on function of linear coupling of microwaves into slots," *High Power Laser Part. Beams*, vol. 15, no. 11, pp. 1093–1099, 2003.

[11] J. Chen and J. Wang, "A three-dimensional semi-implicit FDTD scheme for calculation of shielding effectiveness of enclosure with thin slots," *IEEE Trans. Electromagn. Compat.*, vol. 49, no. 2, pp. 354–360, May 2007.

[12] J. Chen and J. Wang, "Three-dimensional dispersive hybrid implicit–explicit finite-difference time-domain method for simulations of graphene," *Comput. Phys. Commun.*, vol. 207, pp. 211–216, 2016.

[13] J. Chen, J. Guo, and C. Tian, "Analyzing the shielding effectiveness of a graphene-coated shielding sheet by using the HIE-FDTD method," *IEEE Trans. Electromagn. Compat.*, vol. 60, no. 2, pp. 362–367, Apr. 2018.

[14] Z. Liu and X. Wang, "FDTD numerical calculation of shielding effectiveness of electromagnetic shielding fabric based on warp and weft weave points," *IEEE Trans. Electromagn. Compat.*, vol. 62, no. 5, pp. 1693–1702, Oct. 2020.

[15] M. Feliziani, "A FEM approach to shielding effectiveness in braided-shield cables," *IEEE Trans. Magn.*, vol. 26, no. 2, pp. 929–932, Mar. 1990.

[16] L. Hasselgren, E. Moller, and Y. Hamnerius, "Calculation of magnetic shielding of a substation at power frequency using FEM," *IEEE Trans. Power Del.*, vol. 9, no. 3, pp. 1398–1405, Jul. 1994.

[17] M. Maddah-Ali, S. H. H. Sadeghi, and M. Dehmollaian, "Efficient method for calculating the shielding effectiveness of axisymmetric multilayered composite enclosures," *IEEE Trans. Electromagn. Compat.*, vol. 62, no. 1, pp. 218–228, Feb. 2020.

Authorized licensed use limited to: CHINA UNIVERSITY OF MINING AND TECHNOLOGY. Downloaded on February 02,2023 at 00:44:04 UTC from IEEE Xplore. Restrictions apply.

This article has been accepted for inclusion in a future issue of this journal. Content is final as presented, with the exception of pagination.

[18] M. Nazari, R. Moini, S. Fortin, and F. P. Dawalibi, "On the performance of grounding, bonding, and shielding systems for direct and indirect lightning strikes," *IEEE Trans. Electromagn. Compat.*, vol. 62, no. 1, pp. 135–143, Feb. 2020.

[19] H. Pienaar, H. C. Reader, and D. B. Davidson, "Karoo array telescope berm shielding: Efficient computational modeling and multicopter measurement," *IEEE Trans. Electromagn. Compat.*, vol. 59, no. 2, pp. 375–382, Apr. 2017.

[20] H. B. Yuan, W. T. Bao, C. H. Lee, B. F. Zinser, S. Campione, and J. F. Lee, "A method of moments wide band adaptive rational interpolation method for high-quality factor resonant cavities," *IEEE Trans. Antennas Propag.*, vol. 70, no. 5, pp. 3595–3604, May 2022.

[21] K. Chen, P. A. Du, B. L. Nie, and D. Ren, "An improved MoM approach to determine the shielding properties of a rectangular enclosure with a doubly periodic array of apertures," *IEEE Trans. Electromagn. Compat.*, vol. 58, no. 5, pp. 1456–1464, Oct. 2016.

[22] R. Araneo and S. Celozzi, "Toward a definition of the shielding effectiveness in the time-domain," in *Proc. IEEE Int. Symp. Electromagn. Compat.*, 2013, pp. 113–117.

[23] S. Celozzi and R. Araneo, "Alternative definitions for the time-domain shielding effectiveness of enclosures," *IEEE Trans. Electromagn. Compat.*, vol. 56, no. 2, pp. 482–485, Apr. 2014.

[24] A. Tatematsu, F. Rachidi, and M. Rubinstein, "Analysis of electromagnetic fields inside a reinforced concrete building with layered reinforcing bar due to direct and indirect lightning strikes using the FDTD method," *IEEE Trans. Electromagn. Compat.*, vol. 57, no. 3, pp. 405–417, Jun. 2015.

[25] L. Cao, Y. Z. Xie, and M. X. Gao, "Analysis of time-domain shielding effectiveness of enclosures above lossy half-space using an improved half-space FDTD method," *IEEE Trans. Electromagn. Compat.*, vol. 62, no. 5, pp. 2076–2083, Oct. 2020.

[26] Y. Wang, J. Wang, Z. Chen, G. Cheng, and P. Wang, "Three-dimensional simple conformal symplectic particle-in-cell methods for simulations of high power microwave devices," *Comput. Phys. Commun.*, vol. 205, pp. 1–12, Aug. 2016.

[27] K. Fan, B. Wei, and X. He, "A subgridding unconditionally stable FETD method based on local eigenvalue solution," *IEEE Trans. Antennas Propag.*, vol. 69, no. 8, pp. 4695–4705, Aug. 2021.

[28] K. Chen, J. Liu, M. Zhuang, Q. Sun, and Q. H. Liu, "New mixed SETD and FETD methods to overcome the low-frequency breakdown problems by tree-cotree splitting," *IEEE Trans. Microw. Theory Techn.*, vol. 68, no. 8, pp. 3219–3228, Aug. 2020.

[29] K. Chen, X. Hou, M. Zhuang, N. Liu, and Q. H. Liu, "An efficient mixed finite-element time-domain method for complex electrically small problems," *IEEE Trans. Microw. Theory Techn.*, vol. 67, no. 4, pp. 1285–1294, Apr. 2019.

[30] H. Qi, X. Wang, J. Zhang, and J. Wang, "An ADER discontinuous Galerkin method with local time-stepping for transient electromagnetics," *Comput. Phys. Commun.*, vol. 229, pp. 106–115, 2018.

[31] H. Qi, Y. Wang, J. Zhang, X. Wang, and J. Wang, "A partially staggered discontinuous Galerkin method for transient electromagnetics," *J. Comput. Phys.*, vol. 387, pp. 30–44, 2019.

[32] H. Qi, Y. Wang, J. Zhang, X. Wang, and J. Wang, "Explicit high-order exponential time integrator for discontinuous Galerkin solution of Maxwell's equations," *Comput. Phys. Commun.*, vol. 267, 2021, Art. no. 108080.

[33] G. Karypis and V. Kumar, "A fast and highly quality multilevel scheme for partitioning irregular graphs," *SIAM J. Sci. Comput.*, vol. 20, no. 1, pp. 359–392, 1999.

[34] L. S. Andersen and J. L. Volakis, "Hierarchical tangential vector finite elements for tetrahedra," *IEEE Microw. Guided Wave Lett.*, vol. 8, no. 3, pp. 127–129, Mar. 1998.

[35] J. Webb, "Hierarchal vector basis functions of arbitrary order for triangular and tetrahedral finite elements," *IEEE Trans. Antennas Propag.*, vol. 47, no. 8, pp. 1244–1253, Aug. 1999.

[36] S. D. Gedney et al., "The discontinuous Galerkin finite element time domain method (DGFETD)," in *Proc. IEEE Int. Symp. Electromagn. Compat.*, 2008, pp. 1–4.

[37] S. D. Gedney, "An anisotropic PML absorbingmedia for the FDTD simulation of fields in lossy and dispersive media," *Electromagnetics*, vol. 16, no. 4, pp. 399–415, 2007.

[38] E. Montseny, S. Pernet, X. Ferriéres, and G. Cohen, "Dissipative terms and local time-stepping improvements in a spatial high order discontinuous Galerkin scheme for the time-domain Maxwell's equations," *J. Comput. Phys.*, vol. 227, no. 14, pp. 6795–6820, 2008.

[39] G. Cohen, X. Ferrieres, and S. Pernet, "A spatial high-order hexahedral discontinuous Galerkin method to solve Maxwell's equations in time domain," *J. Comput. Phys.*, vol. 217, no. 2, pp. 340–363, 2006.

[40] C. P. Lin, S. Yan, R. R. Arslanbekov, V. Kolobov, and J. M. Jin, "A DGTD algorithm with dynamic h-adaptation and local time-stepping for solving Maxwell's equations," in *Proc. IEEE Antennas Propag. Symp.*, 2016, pp. 2079–2080.

[41] L. Fezoui, S. Lanteri, S. Lohrengel, and S. Piperno, "Convergence and stability of a discontinuous Galerkin time-domain method for the 3D heterogeneous maxwell equations on unstructured meshes," *ESAIM: M2AN*, vol. 39, no. 6, pp. 1149–1176, 2005.

[42] R. Araneo, G. Lovat, and S. Paulotto, "Effects of aperture thickness on the shielding effectiveness of metallic enclosures," in *Proc. IEEE Int. Symp. Electromagn. Compat.*, 2007, pp. 1–3.

[43] M. Li, J. Nuebel, J. L. Drewniak, R. E. DuBroff, T. H. Hubing, and T. P. Van Doren, "EMI from airflow aperture arrays in shielding enclosures-experiments, FDTD, and MoM modeling," *IEEE Trans. Electromagn. Compat.*, vol. 42, no. 3, pp. 265–275, Aug. 2000.

Zheng Lang Jia received the B.S. degree in electronic and information engineering in 2020 from Xidian University, Xi'an, China, where he is currently working toward the M.S. degree.

His current research interests include multiphysics simulation, computational electromagnetics, and electromagnetic compatibility.

Huan Huan Zhang (Senior Member, IEEE) received the Ph.D. degree in electromagnetic fields and microwave technology from the Nanjing University of Science and Technology, Nanjing, China, in 2015.

From 2015 to 2016, he was a Postdoctoral Research Fellow with the Center of Electromagnetics and Optics, The University of Hong Kong, Hong Kong. He is currently an Associate Professor with the School of Electronic Engineering, Xidian University, Xi'an, China. His current research interests include multiphysics simulation, antenna theory, electromagnetic compatibility, and computational electromagnetics.

Dr. Zhang was the recipient of the 2019 Young Scientist Award of the International Applied Computational Electromagnetics Society Symposium. He is a Reviewer of IEEE TRANSACTIONS ON ANTENNA AND PROPAGATION, IEEE ACCESS, *Communications in Computational Physics*, IEEE ANTENNAS AND WIRELESS PROPAGATION LETTERS, IEEE MICROWAVE AND WIRELESS COMPONENTS LETTERS, *IET Radar, Sonar and Navigation*, and *Applied Computational Electromagnetic Society Journal*.

Da Zhi Ding (Senior Member, IEEE) received the B.Sc. and Ph.D. degrees in electromagnetic field and microwave technique from the Nanjing University of Science and Technology (NJUST), Nanjing, China, in 2002 and 2007, respectively.

In 2005, he was a Research Assistant with the Center of wireless Communication, City University of Hong Kong, Hong Kong. He then joined the Department of Electrical Engineering, NJUST, where he became a Lecturer in 2007, a Full Professor in 2014, and the Head of the Department of Communication Engineering in September 2014. He is the author or coauthor of more than 30 technical papers. He has authored or coauthored more than 80 papers. His current research interests include computational electromagnetics, electromagnetic scattering, and radiation.

Dr. Ding is the recipient of the Foundation for China Distinguished Young Investigators presented by the National Science Foundation of China in 2020.

Authorized licensed use limited to: CHINA UNIVERSITY OF MINING AND TECHNOLOGY. Downloaded on February 02,2023 at 00:44:04 UTC from IEEE Xplore. Restrictions apply.

This article has been accepted for inclusion in a future issue of this journal. Content is final as presented, with the exception of pagination.

Lei Zhao (Senior Member, IEEE) received the B.S. degree in mathematics from Jiangsu Normal University, Xuzhou, China, in 1997, and the M.S. degree in computational mathematics and the Ph.D. degree in electromagnetic fields and microwave technology from Southeast University, Nanjing, China, in 2004 and 2007, respectively.

From August 2007 to August 2009, he was a Research Associate with the Department of Electronic Engineering, The Chinese University of Hong Kong, Hong Kong. From September 2009 to December 2018, he was with Jiangsu Normal University, Xuzhou. From February 2011 to April 2011, he was a Research Fellow with the Department of Electrical and Computer Engineering, National University of Singapore, Singapore. From September 2016 to September 2017, he was a Visiting Scholar with the Department of Electrical and Computer Engineering, University of Illinois at Urbana–Champaign, Champaign, IL, USA. Since 2019, he has been with the China University of Mining and Technology, Xuzhou, where he is currently a Full Professor. He has authored and coauthored more than 70 refereed journal and conference papers. His current research interests include spoof surface plasmon polaritons theory and its applications, radio frequency/microwave antenna and filter design, computational electromagnetics, and electromagnetic radiation to humans body.

Dr. Zhao is an Associate Editor for IEEE ACCESS, an Associate Editor-in-Chief for *Applied Computational Electromagnetics Society Journal*, and a Reviewer for multiple journals and conferences, including IEEE TRANSACTIONS ON MICROWAVE THEORY AND TECHNIQUES, IEEE TRANSACTIONS ANTENNAS AND PROPAGATION, IEEE ACCESS, IEEE ANTENNAS AND WIRELESS PROPAGATION LETTERS, *Applied Computational Electromagnetics Society Journal*, and other primary electromagnetics and microwave-related journals.

Qiang Ren (Senior Member, IEEE) received the B.S. degree from Beihang University, Beijing, China, in 2008, the M.S. degree from the Institute of Acoustics, Chinese Academy of Sciences, Beijing, China, in 2011, and the Ph.D. degree from Duke University, Durham, NC, USA, in 2015, all in electrical engineering.

From 2016 to 2017, he was a Postdoctoral Researcher with the Computational Electromagnetics and Antennas Research Laboratory, Pennsylvania State University, University Park, PA, USA. In September 2017, he joined the School of Electronics and Information Engineering, Beihang University, as an Excellent Hundred Associate Professor. He is a Reviewer of more than 30 journals. He has authored or coauthored more than 90 papers in peer-reviewed journals and conferences. His current research interests include numerical modeling methods for complex media, multiscale and multiphysics problems, inverse scattering, deep learning, and parallel computing.

Dr. Ren is the recipient of the Applied Computational Electromagnetics Society (ACES) Early Career Award in 2021, the Young Scientist Award of APEMC 2022, and the Young Scientist Award of 2018 International ACES Symposium in China. He is the Associate Editor for IEEE JOURNAL OF MULTISCALE AND MULTIPHYSICS SIMULATION TECHNIQUES, *ACES Journal*, and *Microwave and Optical Technology Letters*. The students he advised have received multiple awards including Best Student Paper 3rd Prize of PIERS 2021 and Best Paper Shortlist of 2021 Cross Strait Radio Science and Wireless Technology Conference, and Honorable Mention Award of 2022 2022 IEEE International Symposium on Antennas and Propagation and USNC URSI Radio Science Meeting.

Li Jun Jiang (Fellow, IEEE) received the bachelor's degree from the Beijing University of Aeronautics and Astronautics, Beijing, China, in 1993, the master's degree from Tsinghua University, Beijing, in 1996, and the Ph.D. degree from the University of Illinois at Urbana–Champaign (UIUC), Champaign, IL, USA, in 2004, all in electrical engineering.

From 1996 to 1999, he was an Application Engineer with the Hewlett-Packard Company, Palo Alto, CA, USA. From 2004 to 2009, he was the Postdoctoral Research Staff Member and Senior Engineer with IBM T. J. Watson Research Center, Yorktown Heights, NY, USA. In December 2009, he was the Associate Professor and then the Honorable Associate Professor with the Department of Electrical and Electronic Engineering, The University of Hong Kong, Hong Kong, where he received tenure in July 2014. From June 2013 to June 2014, he was the Senior Visiting Professor with Tsinghua University, Beijing, China. From 2014 to 2018, he was an occasional Visiting Scholar to Professor T. Itohs Group with the University of California, Los Angeles, CA, where he spent his Sabbatical from September 2014 to March 2015. In September 2022, he joined the Department of Electronic Engineering, The Chinese University of Hong Kong, Hong Kong, as a Professor and the Associate Director of the Center for Intelligent Electromagnetic Systems. He also has much industrial experience in radio frequency/microwave and signal integrity (SI)/power integrity (PI)/electromagnetic compatibility (EMC) engineering. He has served many top international conferences in his research area as Technical Program Committee Chair, Session Chair, Organization Committee Member, or Session Chair. His multidisciplinary research activities have resulted in leading research outputs around 170 peer-reviewed journal publications, many international and regional awards, multiple patents, and book/book chapters. His research interests include heterogeneous electromagnetic modeling methodologies, high-speed electronic physical design, and electronic design automation solutions, including SI/PI and EMC/electromagnetic interference, antenna and microwave technologies, microwave engineering for linear and nonlinear artificial materials, nanostructures, terahertz, and optics.

Dr. Jiang received the IEEE Technical Achievement Award, the IBM Research Technical Achievement Award, the UIUC Y.T.Lo Outstanding Research Award, and the HP STAR Award. He is the Chair of the IEEE Asia-Pacific International Symposium on Electromagnetic Compatibility International Steering Committee and the Chair of IEEE (Hong Kong) EMC Chapter. He was an Associate Editor or Guest Associate Editor for IEEE TRANSACTIONS ON ANTENNAS AND PROPAGATION, PROCEEDING OF IEEE, and IEEE TRANSACTIONS ON MICROWAVE THEORY AND TECHNIQUES. He was a Member of the IEEE Antennas and Propagation Society Award Selection Committee from 2020 to 2022. He is a Fellow of the Applied Computational Electromagnetics Society.

Authorized licensed use limited to: CHINA UNIVERSITY OF MINING AND TECHNOLOGY. Downloaded on February 02,2023 at 00:44:04 UTC from IEEE Xplore. Restrictions apply.